



HAL
open science

Iron chromium potential to model high-chromium ferritic alloys

Giovanni Bonny, Roberto C Pasianot, Dmitry Terentyev, Lorenzo Malerba

► **To cite this version:**

Giovanni Bonny, Roberto C Pasianot, Dmitry Terentyev, Lorenzo Malerba. Iron chromium potential to model high-chromium ferritic alloys. *Philosophical Magazine*, 2011, pp.1. 10.1080/14786435.2010.545780 . hal-00667589

HAL Id: hal-00667589

<https://hal.science/hal-00667589>

Submitted on 8 Feb 2012

HAL is a multi-disciplinary open access archive for the deposit and dissemination of scientific research documents, whether they are published or not. The documents may come from teaching and research institutions in France or abroad, or from public or private research centers.

L'archive ouverte pluridisciplinaire **HAL**, est destinée au dépôt et à la diffusion de documents scientifiques de niveau recherche, publiés ou non, émanant des établissements d'enseignement et de recherche français ou étrangers, des laboratoires publics ou privés.



Iron chromium potential to model high-chromium ferritic alloys

Journal:	<i>Philosophical Magazine & Philosophical Magazine Letters</i>
Manuscript ID:	TPHM-10-Sep-0405.R2
Journal Selection:	Philosophical Magazine
Date Submitted by the Author:	02-Dec-2010
Complete List of Authors:	Bonny, Giovanni; SCK-CEN, Nuclear Materials Science Institute Pasianot, Roberto; CNEA Terentyev, Dmitry; SCK-CEN Malerba, Lorenzo; SCK-CEN
Keywords:	interatomic potential, atomistic simulation, thermodynamics, dislocations
Keywords (user supplied):	iron chromium alloys

SCHOLARONE™
Manuscripts

Iron chromium potential to model high-chromium ferritic alloys

G. Bonny^{1*}, R.C. Pasianot^{2,3,4}, D. Terentyev¹ and L. Malerba¹

¹SCK•CEN, Nuclear Material Science Institute, Boeretang 200, B-2400, Mol, Belgium

²CAC-CNEA, Depto. de Materiales, Avda. Gral. Paz 1499, 1650 San Martín, Pcia. Buenos Aires, Argentina

³CONICET, Avda. Rivadavia 1917, 1033 Buenos Aires, Argentina

⁴UNSAM/CNEA, Intituto Sabato, Avda. Gral. Paz 1499, 1650 San Martín, Pcia. Buenos Aires, Argentina

Abstract

In this paper we present an Fe-Cr interatomic potential to model high-Cr ferritic steels. The potential is fitted to thermodynamic and point-defect properties obtained from density functional theory (DFT) calculations and experiments. The here developed potential is also benchmarked against other potentials available in literature. It shows particularly good agreement with the DFT obtained mixing enthalpy of the random alloy, the formation energy of intermetallics and experimental excess vibrational entropy and phase diagram. Also DFT calculated point-defect properties, both interstitial and substitutional, are well reproduced as is the screw dislocation core structure. As a first validation of the potential we study the precipitation hardening of Fe-Cr alloys by means of static simulations of the interaction between Cr precipitates and screw dislocations. It is concluded that the description of the dislocation core modification near a precipitate might have a significant influence on the interaction mechanisms observed in dynamic simulations.

Keywords: interatomic potential; atomistic modelling; iron chromium alloys; thermodynamics; dislocations

PACS: 81.30.-t; 81.40.Cd; 61.72.J-; 61.72.Lk

1. Introduction

High-chromium ferritic-martensitic steels (~9-12 at.% Cr) are the materials of choice for high temperature applications in aggressive environments (e.g. corrosion and/or irradiation). As a

1 consequence, they are the commonly proposed structural materials for advanced nuclear
2 reactors. This choice is supported by their superior thermal, corrosion and radiation resistance
3 as compared to austenitic steels. A first approximation to describe such steels in a modelling
4 framework is the Fe-Cr binary alloy.
5

6
7 The addition of chromium to iron influences significantly the response to irradiation. It
8 has been shown that the swelling in Fe-Cr is about one order of magnitude lower than in pure
9 Fe for the same dose [1; 2; 3; 4; 5]. A remarkable effect of Cr is also reported in the shift of
10 the ductile-to-brittle transition temperature (DBTT) in irradiated ferritic-martensitic steels.
11 This shift is found to reach a minimum around 9 at.% Cr [6; 7], in a range of irradiation
12 temperatures from 300 to 410°C and for doses from 7 to 36 dpa. This result is in fact an
13 important reason for choosing Cr concentrations around 9 at.% in most steels proposed for
14 nuclear applications [7].
15

16
17 Even in the absence of irradiation, the Fe-Cr system exhibits a number of peculiarities.
18 Density functional theory (DFT) calculations have shown that the mixing enthalpy exhibits a
19 change of sign [8; 9; 10; 11; 12; 13; 14], which is negative below a critical concentration of
20 ~10 at.% Cr and positive above it. A negative mixing enthalpy indicates solubility and a
21 tendency to partial ordering, while a positive value indicates that Cr atoms cluster into a
22 separate Cr-rich phase (α' phase). These results are compatible with experimental
23 observations that show an inversion of sign of the short-range order (SRO) parameter from
24 negative to positive, with the zero crossing occurring at about 10 at.% Cr [15; 16; 17].
25 However, this behaviour is not reflected in the standard Fe-Cr equilibrium phase diagram
26 [18], whose revision was therefore recently proposed [19] by shifting the concentration of the
27 Fe-rich phase boundary of the meta-stable (when ignoring the sigma phase) miscibility gap to
28 a larger Cr value (~8 at.% Cr), even at low temperature.
29

30
31 In order to better understand the behaviour of Fe-Cr alloys under irradiation, a
32 description at the atomic level is necessary. To address problems of technological interest
33 (e.g. plastic flow behaviour and evolution of the nano- and microstructure), however,
34 descriptions at larger time and space scales are necessary. Both small and large-scale
35 atomistic simulations essentially depend on the interatomic potentials employed, which
36 therefore must strike a balance between the conflicting needs of computational speed and
37 reliability. Thus, an interatomic potential describing the Fe-Cr alloy reasonably well in the
38 temperature range of interest is needed.
39
40
41
42
43
44
45
46
47
48

49 * Author for correspondence. Email: gbonny@sckcen.be; Tel.: +32-14-333197; fax: +32-14-321216.

1 Fe-Cr's complex behaviour is related to magnetic interactions [11]. Yet, in the literature
 2 two interatomic potentials have been developed in an embedded atom method (EAM) like
 3 formalism, which are capable of reproducing Fe-Cr's heat of mixing behaviour as a function
 4 of composition, even without explicitly introducing magnetism. Although both formalisms
 5 succeed at describing the complexity of the ferro-magnetic phase in an effective way,
 6 temperature dependent effects attributed to magnetic transitions cannot be captured within
 7 these models. These are the two-band model (2BM) potential developed by Olsson *et al.* [20]
 8 (henceforth OLS) and the concentration dependent model (CDM) potential developed by Caro
 9 *et al.* [21] (henceforth CAR). Both formalisms are adaptations of the EAM introducing local
 10 concentration dependence. Both potentials, however, suffer from some important drawbacks
 11 regarding thermodynamic properties, point-defect properties and description of screw-
 12 dislocations. In this work, we develop a 2BM potential to correct those short-comings, while
 13 keeping the known useful qualities of both potentials.

14 The paper is organized as follows. In **section 2** we describe the 2BM formalism and the
 15 fitting methodology used; in **section 3**, calculated properties for the pure potentials are
 16 presented and compared with existing potentials. **Sections 4 and 5** report, respectively,
 17 thermodynamic and point-defect properties of our potential, and compare them to experiment
 18 and DFT data; also included is a comparison against OLS (strictly, the one fitted to PAW data
 19 from [20; 22]) and CAR. In **section 6**, as a first application of our potential, we study Cr
 20 precipitation hardening by analysing the interaction between a screw dislocation and a Cr-
 21 precipitate. Finally, **section 7** summarizes the advantages and drawbacks of the different
 22 potentials.

2. Formalism and Fitting Methodology

23 It has been shown that both the 2BM and the CDM formalisms are adequate models to
 24 describe Fe-Cr's complex mixing enthalpy without accounting for magnetism explicitly [23].
 25 Here we choose the 2BM formalism, where the total energy is given as in the EAM with an
 26 extra embedding term, F^s ,

$$E = \frac{1}{2} \sum_{i,j(i \neq j)} V_{t_i t_j}(r_{ij}) + \sum_i F_{t_i}^d(\rho_i^d) + \sum_i F_{t_i}^s(\rho_i^s), \quad (1)$$

The additional embedding term on the right-hand side is assumed to stem from the s -band electrons, while the standard embedding, F^d , is thought of as resulting from the d -band electrons [20]; t_i denotes the atom type (in our case Fe or Cr) on site i . The electron densities, ρ^d and ρ^s , for the d - and s -band, respectively, are calculated as,

$$\rho_i^\lambda = \sum_{j(j \neq i)} \varphi_{t_i t_j}^\lambda(r_{ij}). \quad (2)$$

Here φ^d and φ^s are the d - and s -density functions, respectively, which comply with the relations,

$$\begin{cases} \varphi_{AA}^d = \varphi_{BA}^d = \varphi_A^d \\ \varphi_{BB}^d = \varphi_{AB}^d = \varphi_B^d \\ \varphi_{AA}^s = \varphi_{BB}^s = 0 \\ \varphi_{AB}^s = \varphi_{BA}^s \end{cases}. \quad (3)$$

This choice is in line with [20] so that the d -density reduces to the EAM density, and the s -density samples the local concentration [23]. In this way the s -embedding terms are only relevant for the alloy, and do not contribute to the pure elements' energy, which keeps the standard EAM expression.

Thus, for the Fe-Cr system and within the 2BM, ten functions need to be determined: V_{FeFe} , F_{Fe}^d , φ_{Fe}^d , V_{CrCr} , F_{Cr}^d , φ_{Cr}^d , V_{FeCr} , F_{Fe}^s , F_{Cr}^s and φ_{FeCr}^s . The first three functions determine the Fe potential, the second three the Cr potential and the last four the mixed Fe-Cr interactions. For pure Fe, we chose the potential developed by Mendeleev *et al.* [24], while the pure Cr potential and the mixed Fe-Cr interactions were fitted as is described further on. As is also better detailed further on, the main reason to refit the potential for pure Cr is to provide a better description of dislocation properties in this metal. Generally, the fitting of an interatomic potential to material properties is a problem of matching data obtained from a trial function to a given data set. This problem can be cast into one of minimizing the overall squared deviation, so-called objective function (OF), between the calculated properties and the associated reference data, possibly also imposing constraints. Within our methodology, those properties become linear in the fitting parameters, reducing the scheme to a quadratic programming problem [25] which is exactly solvable; more details are given below.

2.1. Chromium Potential

Prior to fitting the pair interaction V and the embedding term F , we define a reasonable form for the electron density function φ . For this purpose, a simple Thomas-Fermi screening function is selected, which is shifted and truncated for a smooth cut-off between third and fourth nearest neighbour distance (on the bcc equilibrium crystal),

$$\varphi(x) = \varphi_0 \left(\frac{\exp(-\beta x)}{x} - \frac{\exp(-\beta x_{\text{cut}})}{x_{\text{cut}}} \right) f_{\text{cut}}(x), \quad (4)$$

with $x = r/r_0^{1\text{nn}}$, r the distance in Å, $r_0^{1\text{nn}}$ the nearest neighbour distance for the bcc equilibrium crystal (with lattice parameter $a_0=2.878\text{Å}$), $x_{\text{cut}} = 1.65 r_0^{1\text{nn}}$ the cut-off distance, $j_0=0.0676504617$ a normalization factor and $\beta=5$. The cut-off function f_{cut} is defined as,

$$f_{\text{cut}}(x) = \begin{cases} 1 & , \quad x \leq 1 \\ 1 - \frac{(x-1)^3}{(x_{\text{cut}}-1)^3} & , \quad 1 < x \leq x_{\text{cut}} \\ 0 & , \quad x_{\text{cut}} < x \end{cases} \quad (5)$$

The pair interaction V is parameterized by the cubic spline expansion,

$$V(r) = \sum_{k=1}^N a_k (r_k - r)^3 \Theta(r_k - r), \quad (6)$$

where N denotes the number of knots, a_k are the fitting parameters and Θ the Heaviside unit step function. As explained below, the embedding term F is only available in numerical format.

The essential material properties considered in the fit for pure Cr (anti-ferromagnetic phase unless stated otherwise) are the correct stability of different crystallographic structures, the cohesive energy E_{coh} , the equilibrium lattice constant a_0 , the elastic constants (for cubic lattice structures) C_{11} , C_{12} , C_{44} [26] (paramagnetic phase, see Section 3), and the vacancy formation energy, E_{f}^{V} . In addition to these, we also included in the fit the formation energy of self-interstitial configurations (dumbbells oriented along the $\langle 100 \rangle$, $\langle 110 \rangle$ and $\langle 111 \rangle$)

directions), the vacancy migration energy, E_m^V , the $\{110\} \langle 111 \rangle$ gamma surface cut, γ , and the $\frac{1}{2} \langle 111 \rangle$ screw-dislocation core structure. In particular, the gamma surface cut (~10 points) was fitted through the OF, only using the effective pair potential (i.e. neglecting higher order many-body contributions) [27]. The lattice parameter (zero pressure condition), unrelaxed vacancy formation energy, E_f^V , and the three elastic constants were fitted through equality constraints. The bcc lattice stability against fcc ($E_{\text{coh}}(\text{bcc}) - E_{\text{coh}}(\text{fcc}) > 0$) and the Duesbery & Vitek condition for a compact $\frac{1}{2} \langle 111 \rangle$ screw dislocation core ($\gamma(b/3) - 2 \gamma(b/6) > 0$ [28], with b the length of the burgers vector) were fitted through inequality constraints.

Given the effective pair potential, the embedding function is computed by subtraction from Rose's equation [29], which describes the energy per atom $E(\tilde{a})$ for the lattice under uniform expansion or contraction. The expression as a function of the nearest neighbour distance, r^{1nn} , is given as,

$$E(\tilde{a}) = -E_{\text{coh}}(1 + \tilde{a}) \exp(-\tilde{a}). \quad (7)$$

Here $\tilde{a} = \alpha(r^{\text{1nn}} / r_0^{\text{1nn}} - 1)$ and $\alpha^2 = 9\Omega B / E_{\text{coh}}$, where Ω is the atomic volume and B is the bulk modulus. This embedding function, however, is not the one entering the potential. In order to ensure a smooth behaviour and particularly, to constrain the function curvature to remain positive throughout and decreasing at high density, the former embedding is re-fitted on a discrete number of points (~100) taken as reference data. The fit is performed in a minimum square sense and by a cubic spline expansion (also fulfilling $F'(0)=0$). It is the latter expansion that constitutes the embedding function. The price paid for a smooth behaviour is a violation of Rose's equation; however, in the applications of interest the lattice will never be subjected to the large, uniform contractions and dilations that are probed by Rose's equation. Finally, the last fitting step consisted in accommodating manually (i.e. by trial and error) the short distance region to fit the DFT obtained values for self-interstitial formation energies.

Deleted: $a^2 = 9WB / E_{\text{coh}}$

2.2. Alloy Potential

Given the EAM potentials for the pure elements and prior to fitting V_{FeCr} , F_{Fe}^s and F_{Cr}^s , we define a reasonable form for the s -electron density function ϕ_{FeCr}^s . In line with [20], the square of a 4s-type Slater function is chosen,

$$\varphi_{\text{FeCr}}^s(r) = K r^6 \exp(-2\zeta r) g_{\text{cut}}(r). \quad (8)$$

Here $K=20.34075425$ is a normalisation constant, $\zeta=2.5001$ and g_{cut} is a cut-off function to provide a smooth cut-off between fifth and sixth nearest neighbour distance,

$$g_{\text{cut}}(r) = \begin{cases} 1 & , r \leq r_c^i \\ \frac{1}{2} \left\{ 1 - \sin \left[\frac{\pi}{2} \frac{(r - r_m)}{d} \right] \right\} & , r_c^i < r \leq r_c^f \\ 0 & , r_c^f < r \end{cases} \quad (9)$$

with $r_c^i=5.1\text{\AA}$ the inner cut-off, $r_c^f=5.3\text{\AA}$ the outer cut-off, $r_m = (r_c^i + r_c^f)/2$ and $d = (r_c^f - r_c^i)/2$. The mixed pair interaction V_{FeCr} is parameterized by a cubic spline expansion as in Equation (6) while the s -embedding functions F^s are parameterized by an extended second moment expression similar to [20; 30],

$$F^s(\rho) = A_1 \sqrt{\rho} + A_2 \rho^2, \quad (10)$$

with A_1 and A_2 fitting parameters. The square root proved to be essential in reproducing the correct trends in Cr-Cr and Cr-vacancy interactions. In fact, former attempts using spline expansions as in [23] were met with failure. In this work we normalized the (maximum) s -density in such a way that unity corresponds to a single Cr hosted in the Fe matrix.

The mixed pair interaction, as well as both s -embedding functions, were fitted simultaneously to all properties of interest. The mixing enthalpy was fitted in the whole concentration range (~50 points) using a variance expansion as described in [23], while at each concentration a zero pressure condition was imposed to obtain a lattice parameter as close as possible to the linear interpolation between the equilibrium lattice parameters of the pure elements. In addition, the Cr-Cr and Cr-vacancy interaction energies up to second nearest neighbour were fitted, as well as the Cr-vacancy migration energy in Fe, using DFT reference values as guides [12]. All the mentioned properties were fitted using appropriate weights to obtain reasonable values. In addition to the expansion coefficients of the s -embedding functions and the mixed pair potential, there remains one degree of freedom that expresses the relative weight between the d -densities of Fe and Cr, $\rho_{\text{Fe}}/\rho_{\text{Cr}}$. By manually changing this

1 fraction and consequently solving the quadratic programming problem, we fitted the excess
2 vibrational entropy, computed in the harmonic approximation [31], to a value as close as
3 possible to the experimental one, without losing the above properties and without stabilizing
4 unphysical intermetallic compounds. Finally, the potential was manually adjusted in the short
5 distance region to reproduce the DFT-obtained binding energy of the mixed $\langle 110 \rangle$ Fe-Cr
6 dumbbell. A description of the full Fe-Cr potential is given in [Appendix A](#).
7
8
9

11 3. Properties of the Iron and Chromium Potentials

14 From the EAM-type potentials available in the literature to describe pure Fe that are capable
15 of reproducing the $\langle 110 \rangle$ self-interstitial configuration as the most stable, we considered those
16 from Refs. [24], [32] and [33], finally selecting “potential 2” developed by Mendeleev *et al.*
17 [24], which has been widely used and tested. In [34] it has been demonstrated that the
18 potentials from [24] and [32] succeed best in reproducing the properties of iron that are of
19 interest for radiation damage studies. However, of all, our choice is the only one for which a
20 clear proof exists of being able to consistently describe stable glide of a screw dislocation in a
21 $\{110\}$ plane [35].
22
23
24
25

26 Among the potentials for Cr, we considered those from Refs. [36] and [20]. The latter,
27 henceforth O05, was used in combination with the Fe potential by Ackland *et al.* [32] to
28 produce the OLS and CAR potentials. The basic properties of our potential are summarized
29 and compared to O05 and DFT data in [Table 1](#). There, $B=(C_{11}+2C_{12})/3$ is the bulk modulus,
30 $C'=(C_{11}-C_{12})/2$ is the tetragonal shear and C_{44} is the shear modulus [26]. Clearly, the
31 experimental elastic properties are well reproduced by both potentials. Note, however, that at
32 zero Kelvin Cr is anti-ferromagnetic and has a negative Cauchy pressure [37], which cannot
33 be reproduced within a standard central force framework [38; 39; 40]. Above its Néel
34 temperature (~ 310 K), however, Cr is paramagnetic with a positive Cauchy pressure [41].
35 Since we focus on technological applications above room temperatures, our potential was
36 fitted to the elastic constants of paramagnetic Cr, linearly extrapolated down to zero Kelvin
37 (the values given in [Table 1](#), see e.g. [36]). Furthermore, our potential also closely fits a_0 , E_f^V ,
38 E_{coh} and E_m^V , obtaining improved values for the latter two. The relative stability between the
39 different self interstitial configurations is not equally well reproduced as by O05, but the
40 important trends given by DFT are reproduced, i.e., the $\langle 110 \rangle$ and $\langle 111 \rangle$ configurations are
41 almost degenerate and more stable than the $\langle 100 \rangle$ configuration. Finally, our potential is closer
42
43
44
45
46
47
48
49
50
51
52
53
54
55
56
57
58
59
60

1 to DFT data regarding the energy difference between the body-centred cubic (bcc) and face-
2 centred cubic (fcc) phase, thus providing enhanced stability of the bcc phase at high
3 temperature. In summary, from the values presented in **Table 1** we can conclude that the basic
4 properties of Cr are equally well reproduced by both potentials.
5
6

7
8 *Insert table 1 around here*
9

10
11 The O05 potential, however, does not reproduce the correct structure for a $\frac{1}{2}$ $\langle 111 \rangle$
12 screw-dislocation core, which is the main reason to refit the Cr potential. This is depicted in
13 **Figure 1** via differential displacement maps [42]. Clearly O05 shows a three-fold symmetry
14 core, opposite to the compact one, as predicted by DFT [43] and our potential.
15
16

17
18 *Insert figure 1 around here*
19

20 21 **4. Thermodynamic Properties**

22
23 Prior to presenting the phase diagrams resulting from the different potentials, we compare and
24 discuss statically calculated properties that influence the Fe-Cr phase diagram. In **Figure 2** the
25 mixing enthalpy calculated with the three potentials is compared to DFT data [8; 12; 44]. For
26 the mixing enthalpy resulting from the potentials 50 compositions in the complete
27 concentration range were sampled. For each composition the solutes were randomly
28 distributed in cubic bcc crystals containing 2000 atoms and relaxed at constant pressure using
29 a conjugate gradient method. Although different DFT techniques give different values for the
30 mixing enthalpy, the DFT curves show the same behaviour, i.e., a change of sign in the
31 mixing enthalpy, being negative below ~ 5 at.% Cr and positive above. Both 2BM potentials
32 were fitted to DFT data [12; 44] obtained from special quasi-random structures (SQSs) [45]
33 while CAR was fitted to DFT data [8] obtained from a coherent potential approximation
34 (CPA) [46]. The mixing enthalpy curves from our potential and CAR reproduce the DFT
35 mixing enthalpy very well, both qualitatively and quantitatively. Below ~ 25 at.% Cr this is
36 also true for OLS; the complete curve, however, takes a symmetric shape, in contrast to the
37 asymmetric DFT shape. As a consequence, the mixing enthalpy takes negative values at the
38 Cr-rich side too, leading to short-range order and high Fe solubility in the Cr-rich phase.
39 These observations contradict DFT data and have never been reported in experimental studies.
40
41
42
43
44
45
46
47
48
49
50

1
2
3
4
5
6
7
8
9
10
11
12
13
14
15
16
17
18
19
20
21
22
23
24
25
26
27
28
29
30
31
32
33
34
35
36
37
38
39
40
41
42
43
44
45
46
47
48
49
50
51
52
53
54
55
56
57
58
59
60

Insert figure 2 around here

The formation energy of intermetallic compounds is another issue to be considered. In **Figure 3** the formation energy of 57 intermetallic compounds (as described in [11; 47]) calculated by the three potentials and DFT are compared. In both cases, the configurations were relaxed at constant pressure using a conjugate gradient method. Below 10 at.% Cr DFT predicts stable intermetallic compounds, consistent with the negative mixing enthalpy for the disordered alloy. Above 10 at.% Cr, the formation energy of the intermetallic compounds becomes positive and remains so throughout the composition range.

In the Fe-rich region (< 10 at.% Cr), the most stable compounds predicted by DFT are also the most stable ones predicted by all three potentials (see **Figure 3**), with most importantly the lowest compound at 6.67 at.% Cr. This compound is described by a unit cell with axes oriented along the [210], $[\bar{1}20]$ and [001] directions with dimensions $\sqrt{5}a_0 \times \sqrt{5}a_0 \times 3a_0$. It contains 30 atoms, of which 2 Cr are separated by 7nn distance ($\sqrt{19}/2a_0$) along [133]. It should be noted that this compound is consistent with the ordered phase observed in the Monte Carlo simulations by Pareige et al. [48] using OLS. Among the three, both 2BM potentials also give good quantitative agreement in that concentration range. At higher Cr composition (> 10 at.%), OLS generally overstabilizes the compounds thereby even giving negative values at 50 and 93.33 at.% Cr. The latter is consistent with the low (compared to DFT) and negative mixing enthalpy of the disordered alloy at equiatomic and Cr-rich compositions, respectively. Such negative values in turn may lead to unphysical configurations in the course of e.g. Monte Carlo simulations, and thus constitute a drawback of the potential. The other two potentials do not suffer from the latter problems, although ours still somewhat overstabilizes the compounds.

Insert figure 3 around here

Experiments have shown the excess vibrational entropy to be non-negligible for the Fe-Cr system [49; 50; 51]; also, it was predicted to have a significant influence on the location of the solubility limit [44]. We calculated the excess vibrational entropy with all three potentials for disordered alloys, based on the harmonic approximation [31] in the Γ point applied to cells containing 1024 atoms, prepared as purely random samples.

In **Figure 4** excess vibrational entropies for all three potentials are compared with experimental values for the ferro-magnetic phase [49; 51]. The experimental curves suggest a

1 non-negligible contribution to the total excess entropy, amounting to 30-40% of the
 2 configurational entropy for the disordered alloy. As shown in the figure none of the potentials
 3 gives a close fit to the experimental values. From the three, however, both 2BM potentials
 4 agree best, with ours and OLS closest to the data from [49] and [51], respectively. In the
 5 former case the experimental data is underestimated by a factor of about 1.5; in the latter it is
 6 overestimated (below ~75 at.% Cr) by about the same factor. The CAR potential, on the other
 7 hand, underestimates S_{xc}^{vib} by about a factor 3 and gives negative contributions below ~12
 8 at.% Cr, which contradicts experiments (see also [44; 52]).
 9

10
 11
 12
 13
 14
 15
 16
 17
 18
 19
 20
 21
 22
 23
 24
 25
 26
 27
 28
 29
 30
 31
 32
 33
 34
 35
 36
 37
 38
 39
 40
 41
 42
 43
 44
 45
 46
 47
 48
 49
 50
 51
 52
 53
 54
 55
 56
 57
 58
 59
 60

Insert figure 4 around here

The phase diagrams based on all three potentials are compared to a recently proposed parameterization based on the CALPHAD methodology [53] in **Figure 5**. The CALPHAD miscibility gap is calculated from an experimentally based [53; 54] Gibbs free energy parameterization. To indicate the ferro to paramagnetic phase transition, the CALPHAD calculated Curie temperature is also added. The phase boundaries for our potential and OLS are obtained from isobaric Monte Carlo simulations in the semi-grand canonical ensemble [55]. In the figure the data points are interpolated by smooth curves to guide the eye. These curves are based on the data points and the fact that full solubility was verified to occur starting from 1200K and 800K for our potential and OLS, respectively. The phase boundaries for CAR were obtained from free energy calculations using a thermodynamic integration technique (see [52] for more details). Thus in all cases vibrational and configurational entropy were accounted for.

When focussed on the Fe-rich side, we observe large Cr solubility at low temperature, due to the negative heat of mixing. As shown in **Figure 5**, this behaviour is well reproduced by all potentials, with a particularly close agreement for ours. At about 750K the Fe-rich solubility limit increases until full solubility is observed above the critical temperature ~900K within the CALPHAD calculation. The curve resulting from OLS underestimates this critical temperature by ~200K while our potential overestimates it by roughly the same amount. The critical temperature resulting from CAR, on the other hand, lies above the melting temperature. Note that the difference in critical temperature between OLS and ours closely follows the different trends observed in the excess vibrational entropy. Good agreement of the critical temperature obtained with potentials and CALPHAD should not be expected since magnetic interactions are not explicitly included in the former. Below ~25 at.%, however,

Deleted: .

Deleted:

Deleted: It should be noted that below

1 direct comparison with the Calphad phase diagram is justified since in this concentration
2 range the Calphad phase boundary is well below the Curie temperature. For higher Cr
3 concentrations, however, care should be taken as the magnetic transition might significantly
4 affect the solubility, thus close agreement between experiment and potential prediction might
5 not be a concern for potentials that effectively describe the ferro-magnetic phase.
6
7

8 On the Cr-rich side, the Fe solubility approaches zero with decreasing temperature,
9 which is well reproduced by both our potential and CAR. The OLS potential, on the other
10 hand, predicts high Fe-solubility as an unphysical artefact of the negative heat of mixing at
11 the Cr-rich side.
12
13

14
15
16 *Insert figure 5 around here*
17

18 **5. Point-Defect Properties**

19
20
21 The formation, migration and binding energies reported in the current section were calculated
22 in cubic bcc boxes containing 2000 atoms at constant volume ($a_0=2.8553\text{\AA}$) up to a precision
23 of 1meV. For the formation and binding energies the boxes were relaxed using a conjugate
24 gradient method and the migration energies were estimated using the nudged elastic band
25 method [56].
26
27

28 In **Figure 6** the Cr-Cr and Cr-vacancy interaction energy (E_i) in bulk Fe calculated using
29 the three potentials and DFT [12] is presented. The DFT data show Cr-Cr repulsion in bulk Fe
30 that decreases fast with increasing distance. This behaviour is mainly responsible for the
31 experimentally observed SRO and is acceptably well reproduced by all potentials. Both 2BM
32 potentials, however, underestimate the difference in repulsion between first and second
33 nearest neighbour Cr pairs; an effect that is well reproduced by CAR. Concerning the Cr-
34 vacancy interaction, according to both DFT calculations [12] and experiments [57], it is
35 essentially negligible. As shown in **Figure 6**, this feature is also qualitatively reproduced by
36 all potentials, that predict weak repulsion between Cr and vacancy. It is important, however,
37 that the interaction energy between 1nn and 2nn Cr-vacancy pairs increases, as reproduced by
38 all potentials. This is a prerequisite to obtain the correct order between forward and backward
39 Cr-vacancy exchanges for several chemical environments in the Fe matrix, as discussed
40 further.
41
42
43
44
45
46
47
48

49 *Insert figure 6 around here*
50

1
2
3
4
5
6
7
8
9
10
11
12
13
14
15
16
17
18
19
20
21
22
23
24
25
26
27
28
29
30
31
32
33
34
35
36
37
38
39
40
41
42
43
44
45
46
47
48
49
50
51
52
53
54
55
56
57
58
59
60

In **Figure 7** the average (of forward and backward) vacancy migration barriers for different local Cr configurations calculated with the three potentials are compared to the corresponding DFT values [58]. The DFT results show that the barriers are largest for both Cr and Fe exchanges when there are three Cr and three Fe atoms occupying the six nearest neighbour positions around the saddle-point. This effect is only reproduced by our potential, although OLS and CAR also give reasonable trends. Note, however, that in the case of the CAR potential, the value for Cr migration in bulk Fe is significantly overestimated. As a consequence, Cr migration barriers calculated with CAR are somewhat higher as compared to the corresponding DFT values. For the Fe jumps, on the other hand, the migration barriers are largely underestimated when locally enriched by three or more Cr atoms. For completeness, a table summarizing the precise configurations and values of both forward and backward jumps on which **Figure 8** is based is given in **Appendix B**.

Insert figure 7 around here

In **Figure 8** we show the formation energy of interstitial defects in bulk Fe, taking the $\langle 110 \rangle$ mixed dumbbell as reference; values predicted by DFT [12] and the three potentials are compared. From the DFT data [12] it follows that the $\langle 110 \rangle$ mixed dumbbell configuration in bulk Fe has the lowest formation energy. However, the inclusion of Cr in the defect diminishes the difference in formation energy between the $\langle 111 \rangle$ and $\langle 110 \rangle$ configurations.

In the case of pure Fe, all potentials follow the DFT trend reasonably well, with a proper reproduction of the relative differences between the formation energies of the $\langle 100 \rangle$, $\langle 110 \rangle$ and $\langle 111 \rangle$ configurations being the most important feature. With the introduction of Cr, the data from our potential still captures the shape of the DFT curves reasonably well, while the data from OLS give almost degenerate values for all configurations. The CAR potential, on the other hand, fails to reproduce the $\langle 110 \rangle$ mixed dumbbell as the lowest energy configuration.

Insert figure 8 around here

Next, we compare the binding energy of Cr interstitials in bulk Fe obtained from the three potentials with the corresponding DFT values [12]. Such a comparison is presented in **Figure 9**. As expected from the above results, the CAR potential shows poor agreement with

1 DFT data. Given that both 2BM potentials were only fitted to the binding energy between a
2 single Cr and the $\langle 110 \rangle$ dumbbell, they show reasonable agreement with DFT. In particular,
3 our potential is the only one that correctly reproduces the sign for all reported binding
4 energies.
5
6

7
8
9 *Insert figure 9 around here*

10 11 **6. Dislocation-Precipitate Interaction**

12
13
14 Here we address the problem of dislocations in Fe and Cr and of the interaction of a
15 $\frac{1}{2}\langle 111 \rangle$ screw dislocation with Cr precipitates in the Fe matrix, as obtained from static
16 simulations. The dislocation core energy and radius, shear modulus, Poisson ratio and Peierls
17 stress for a $\frac{1}{2}\langle 111 \rangle$ screw and a $\frac{1}{2}\langle 111 \rangle\{110\}$ edge dislocation in the pure metals are
18 summarized in **Table 2**. Details regarding the calculations can be found in Ref. [59], where
19 the interaction of an edge dislocation with Cr precipitates was characterized. From **Table 2** it
20 appears that the two Fe potentials provide very similar results, whereas the Cr potentials
21 exhibit at least two essential differences. The shear modulus calculated with our potential is
22 $\sim 30\%$ smaller, while the Poisson ratio is two times larger than according to OLS. The
23 characteristics of the core of both edge and screw dislocations are similar with both potentials.
24 Finally, we note that the two Cr potentials predict approximately the same Peierls stress (τ_p)
25 for the screw dislocation, which is higher than τ_p in Fe by 35% and 55% according to OLS
26 and our potentials, respectively.
27
28
29
30
31
32

33
34
35 *Insert table 2 around here*

36
37 The interaction of a screw dislocation with Cr precipitates was studied in a bcc
38 simulation box with dimensions $20 \times 12 \times 28 \text{ nm}^3$ with axes oriented along the $[\bar{1}\bar{1}2]$, $[1\bar{1}0]$
39 and $[111]$ directions. Periodic boundary conditions were applied in the $[111]$ direction and a
40 straight screw dislocation with left-handed thread and Burgers vector $\mathbf{b} = 1/2[111]$ was created.
41 A Cr precipitate was inserted at a defined distance from the dislocation line and placed so that
42 its centre coincides with the $(1\bar{1}0)$ glide plane of the screw dislocation. Then the relaxation
43 was performed to calculate the total energy of the crystal as a function of the distance between
44 the precipitate centre and dislocation line. The precipitate-dislocation interaction energy E_I
45
46
47
48
49
50

1 was estimated as $E_I=(E^{D+P}+E^{Fc})-(E^D-E^P)$, following [60] (positive values indicate repulsive
2 interaction). Here E^{D+P} , E^D and E^P are the total energy of the crystal containing the dislocation
3 interacting with the precipitate, dislocation only and precipitate only, respectively. E^{Fc} is the
4 total energy of the Fe crystal with the same geometry and boundary conditions as the crystals
5 used to calculate the above mentioned energies. All crystals were relaxed to reach a
6 convergence of at least 5meV in the total energy.
7
8

9
10 As mentioned in section 3 the two Cr potentials predict different core structures for the
11 screw dislocation in pure Cr. Therefore it is of interest to investigate whether or not the non-
12 degenerate-to-degenerate core structure modification occurs at the precipitate-matrix interface
13 and inside the precipitate. It should be noted that such a modification was found to occur with
14 OLS in our previous study [61]. To address this issue, the core structure of different
15 dislocation segments, selected according to the scheme presented in Table 3, was constructed
16 using the differential displacement (DD) method [42] from the atomic positions obtained after
17 relaxation. The corresponding DD maps are also presented in Table 3. Firstly, we observe that
18 the core structure of the segment located near the centre of the precipitate was found to be the
19 same as in pure Cr for the corresponding potentials, i.e. the three-fold split core for OLS and
20 isotropic for our potential (Figure 1). The core of the segment penetrating the precipitate
21 normal to its surface (#1 of Table 3) has a two-fold structure with pronounced split over the
22 precipitate surface, similar for both potentials. However, a difference in the core structure was
23 found for the segments penetrating the precipitate at a tangent to its surface (#2 and #3 in
24 Table 3 as the limiting case). With our potential no isotropic or three fold structure
25 modification occurs, contrary to OLS. Additional calculations, not reported here, proved that,
26 with OLS, the isotropic-to-degenerate core transformation occurs not only inside the
27 precipitate but also everywhere near the precipitate matrix interface. The latter implies that in
28 MD simulations such core transformation may manifest itself as emission of kink pairs in the
29 $\{112\}$ plane, thus causing cross-slip movement instead of stable glide (see [43] for details).
30
31
32
33
34
35
36
37
38
39

40 *Insert table 3 around here*
41
42

43 The interaction energy of the dislocation with precipitates of different sizes as a
44 function of distance between precipitate centre and dislocation line is presented in Figure 10.
45 Qualitatively, the curves look similar for both potentials, showing a maximum in the centre of
46 the precipitate and a fast decrease beyond the precipitate radius. Quantitatively, however, the
47 maximum interaction energy estimated with the OLS is about twice as high considering
48
49
50
51
52
53
54
55
56
57
58
59
60

precipitates of the same size. The derivative of the interaction energy with respect to the distance gives an estimate for the interaction force, from which the maximum force (and hence stress) necessary for the dislocation to shear a precipitate can be calculated. Irrespective of the precipitate size and applied potential, the maximum interaction force occurs at ~65% from the precipitate centre.

Insert figure 10 around here

The difference in magnitude of the interaction energy between the two potentials can be attributed to the difference in the shear modulus of pure Cr (see Table 2). For a more correct treatment, however, contributions from the chemical energy (due to additional Fe-Cr interface) and dislocation core energy (which differs in Fe and Cr) should not be neglected. Therefore, we have performed additional calculations allowing the total interaction energy to be decomposed into the contributions coming from the shear modulus misfit, chemical and relaxation (related to the strain created around the precipitate) excess energy. The chemical component, E_S , was calculated statically, by shearing a precipitate in the $(1\bar{1}0)$ plane at its centre by the distance b , in a number of steps, each equal to $2R_p/b$, followed by relaxation. In this way we mimic the shearing of the precipitate due to the advance of the screw dislocation. The shear modulus misfit component, E_μ , was calculated by taking the volume integral of the dislocation strain energy between the particle centred at $(h_x, h_y, 0)$ and a dislocation line parallel to the z axis, following the expression [62]:

$$E_\mu = \frac{\mu_P - \mu_M}{\mu_M} \int_P \rho \cdot D_z(\rho, \theta) \cdot e_M(\rho, \theta) \cdot d\rho \cdot d\theta. \quad (11)$$

Here the subscripts M and P indicate respectively matrix and precipitate, $\rho = \sqrt{x^2 + y^2}$ and $\theta = \arctan(x/y)$ are the standard polar coordinates, $e(\rho, \theta) = \mu b^2 / 8\pi^2 \rho^2$ is the strain energy density and D_z is expressed as:

$$D_z(\rho, \theta) = 2\sqrt{R_p^2 - (\rho \cos \theta - h_x)^2 - (\rho \sin \theta - h_y)^2}. \quad (12)$$

In turn, the excess relaxation energy was calculated as $E_{xc} = E_I - (E_S + E_\mu)$.

1 As a representative example, the three above determined components and their
2 derivatives, calculated for a screw dislocation interacting with a 4 nm precipitate, are shown
3 in **Figure 11**. The smallest contribution comes from the chemical component, whose curve is
4 magnified ten times for better observation while the contribution from the shear modulus
5 misfit clearly dominates. As expected, its absolute contribution is the highest for OLS.
6 Interestingly, the third term, i.e. the relaxation excess energy, appears to be approximately the
7 same and negative for both potentials. In absolute terms, however, E_{xc} is higher for OLS.
8
9
10
11

12 *Insert figure 11 around here*
13
14

15 **7. Summary and Concluding Remarks**

16
17
18 Based on the phase diagram, all potentials are capable of reproducing short-range order
19 and α' precipitation. Our potential, however, seems to be the best compromise for
20 thermodynamic modelling. It gives an asymmetric mixing enthalpy, does not stabilize
21 unobserved intermetallic compounds (unlike OLS), provides (though underestimated) a
22 significant amount of excess vibrational entropy (unlike CAR) and a reasonable agreement
23 with the experimental miscibility gap. [given that magnetic interactions are not explicitly
24 included in the formalism.](#)
25
26
27

28
29 Based on the description of substitutional defect interactions and the phase diagram,
30 both OLS and our potential *a priori* seem to be the most appropriate choice to simulate
31 thermal annealing in Fe-Cr alloys. Besides a proper reproduction of the thermodynamic limit,
32 a reasonable reproduction of vacancy migration barriers, Cr-Cr and Cr-vacancy interactions
33 assure that the correct kinetic path is followed using the correct mechanisms. All potentials
34 provide a reasonable description of the Cr-Cr and Cr-vacancy interactions, but only the 2BM
35 potentials provide reasonable values for vacancy migration barriers, with ours following the
36 DFT trends the closest among the two.
37
38
39

40
41 Based on the description of interstitial and substitutional defect interactions and the
42 phase diagram, both 2BM potentials *a priori* seem to be the most appropriate choice to
43 simulate thermal annealing of Fe-Cr alloys under irradiation. Besides a proper description of
44 thermal annealing, a correct stabilization of interstitial complexes is needed to assure that the
45 correct micro-structure is obtained under irradiation. Both 2BM potentials provide reasonable
46 interstitial stabilities (ours in particular), while CAR poorly reproduces interstitial properties.
47
48
49
50
51
52
53
54
55
56
57
58
59
60

1 Based on the description of the $\frac{1}{2} \langle 111 \rangle$ screw dislocation core structure (in bulk Fe and
2 Cr) and its stable glide in a $\{110\}$ plane in bulk Fe, our potential *a priori* seems to be the most
3 suitable choice for the simulation of precipitate-screw dislocation interaction. From the three
4 potentials, ours is the only one reproducing the compact $\frac{1}{2} \langle 111 \rangle$ screw dislocation core
5 structure in bulk Cr. In addition, our static simulations have revealed an isotropic-to-
6 degenerate core transition in every position near the precipitate with OLS that is not seen with
7 our potential. Such a core modification may lead to different interaction mechanisms in
8 dynamic simulations, such as cross slip.
9

10 In summary, we have shown that the here developed Fe-Cr potential reached the goal of
11 removing the main shortcomings of previously existing ones, while conserving their “good”
12 properties. It should be noted, however, that it is not stiffened to the screened Coulomb
13 interaction and is therefore not suitable to simulate collision cascades in its present form.
14
15
16
17
18
19

20 Acknowledgements

21
22 The authors thank Drs. D. Nguyen-Manh, M.Yu. Lavrentiev and S. Cottenier for fruitful
23 discussions and their help in preparation of this paper. This research has received partial
24 funding from the European Atomic Energy Community’s 7th Framework Programme
25 (FP7/2007-2011), under grant agreement number 212175 (GetMat project). It also contributes
26 to the European Fusion Technology programme (EFDA). The work was partially sponsored
27 by the belgo-argentine MINCYT-FWO bilateral cooperation agreement, Project
28 FW/07/EXII/002. RCP acknowledges support from CONICET-PICT 5062.
29
30
31
32

Deleted: ¶

33 Appendix A: Tabulation of the Potential Functions

34
35
36
37 Tabulations containing up to 5000 points are available on-line as supplementary material
38 related to this paper or at: <http://www.ctcms.nist.gov/potentials/> or upon request to the
39 authors. Note that a tabulation of the *s*-embedding functions is not provided due to the
40 singular slope in the origin, so that care should be exercised if used in tabular form. The
41 parameters for the *s*-embedding functions are $A_1 = -0.217009784$, $A_2 = 0.388002579$ and $A_1 = -$
42 0.00977557632 , $A_2 = 0.374570104$ for Fe and Cr, respectively.
43
44
45
46

47 Appendix B: Vacancy Migration Barriers

1 In this appendix the migration barriers for Fe-Vacancy and Cr-Vacancy exchange for different
2 local chemical environments are provided. The latter are built by adding Cr atoms at the six
3 nearest neighbour positions around the migration saddle point. The details are as reported in
4 Table B-1 next.
5
6
7

Deleted: d

8 *Insert table B-1 around here*
9

11 References

- 12
13
14 [1]E.A. Little, Journal of Nuclear Materials 87 (1979) 11.
15 [2]E.A. Little, D.A. Stow, Metal Science 14 (1980) 89.
16 [3]S. Porollo, A. Dvoriashin, A. Vorobyev, Y. Konobeev, Journal of Nuclear Materials 256
17 (1998) 247.
18 [4]F.A. Garner, M.B. Toloczko, B.H. Sencer, Journal of Nuclear Materials 276 (2000) 123.
19 [5]Y. Konobeev, A. Dvoriashin, S. Porollo, F. Garner, Journal of Nuclear Materials 355
20 (2006) 124.
21 [6]H. Kayano, A. Kimura, M. Narui, Y. Sasaki, K. Suzuki, S. Ohta, Journal of Nuclear
22 Materials 155-157 (1988) 978.
23 [7]A. Kohyama, A. Hishinuma, D.S. Gelles, R.L. Klueh, W. Dietz, K. Ehrlich, Journal of
24 Nuclear Materials 233 (1996) 138.
25 [8]P. Olsson, I. Abrikosov, L. Vitos, J. Wallenius, Journal of Nuclear Materials 321 (2003)
26 84.
27 [9]A.A. Mirzoev, M.M. Yalalov, D.A. Mirzaev, Physics of Metals and Metallography 97
28 (2004) 336.
29 [10]P. Olsson, I.A. Abrikosov, J. Wallenius, Physical Review B 73 (2006) 8.
30 [11]T.P.C. Klaver, R. Drautz, M.W. Finnis, Physical Review B 74 (2006) 094435.
31 [12]P. Olsson, C. Domain, J. Wallenius, Physical Review B 75 (2007) 014110.
32 [13]D. Nguyen-Manh, M.Y. Lavrentiev, S.L. Dudarev, Journal of Computer-Aided Materials
33 Design 14 (2007) 159.
34 [14]P. Erhart, B. Sadigh, A. Caro, Applied Physics Letters 92 (2008) 3.
35 [15]I. Mirebeau, M. Hennion, G. Parette, Physical Review Letters 53 (1984) 687.
36 [16]N.P. Filippova, V.A. Shabashov, A.L. Nikolaev, Physics of Metals and Metallography 90
37 (2000) 145.
38
39
40
41
42
43
44
45
46
47
48
49
50
51
52
53
54
55
56
57
58
59
60

- 1 [17]V.V. Sagaradze, Kositsyna, II, V.L. Arbutov, V.A. Shabashov, Y.I. Filippov, Physics of
2 Metals and Metallography 92 (2001) 508.
- 3 [18]J.O. Andersson, B. Sundman, Calphad-Computer Coupling of Phase Diagrams and
4 Thermochemistry 11 (1987) 83.
- 5 [19]G. Bonny, D. Terentyev, L. Malerba, Scripta Materialia 59 (2008) 1193.
- 6 [20]P. Olsson, J. Wallenius, C. Domain, K. Nordlund, L. Malerba, Physical Review B 72
7 (2005) 214119.
- 8 [21]A. Caro, D.A. Crowson, M. Caro, Physical Review Letters 95 (2005) 75702.
- 9 [22]P. Olsson, J. Wallenius, C. Domain, K. Nordlund, L. Malerba, Physical Review B 74
10 (2006) 1(E).
- 11 [23]G. Bonny, R. Pasianot, L. Malerba, Philosophical Magazine 89 (2009) 711.
- 12 [24]M. Mendeleev, S. Han, D. Srolovitz, Philosophical Magazine 83 (2003) 3977.
- 13 [25]J. Nocedal, S.J. Wright, Numerical Optimization, Springer-Verlag, New York, 2006.
- 14 [26]C. Kittel, Introduction to Solid State Physics, John Wiley & Sons, New York, 1996.
- 15 [27]M. Finnis, E. Sinclair, Philosophical Magazine A 50 (1984) 45.
- 16 [28]M.S. Duesbery, V. Vitek, Acta Materialia 46 (1998) 1481.
- 17 [29]J.H. Rose, J.R. Smith, F. Guinea, J. Ferrante, Physical Review B 29 (1984) 2963.
- 18 [30]G.J. Ackland, S.K. Reed, Physical Review B 67 (2003) 174108.
- 19 [31]A. Walle van de, G. Ceder, Reviews of Modern Physics 74 (2002) 11.
- 20 [32]G. Ackland, M. Mendeleev, D. Srolovitz, S. Han, A. Barashev, Journal of Physics:
21 Condensed Matter 16 (2004) 1.
- 22 [33]S. Dudarev, P. Derlet, Journal of Physics: Condensed Matter 17 (2005) 1.
- 23 [34]L. Malerba, et al., Journal of Nuclear Materials [406\(2010\) 19](#).
- 24 [35]C. Domain, G. Monnet, Physical Review Letters 95 (2005) 215506.
- 25 [36]J. Wallenius, I. Abrikosov, R. Chakarova, C. Lagerstedt, L. Malerba, P. Olsson, V.
26 Pontikis, B. Sadigh, D. Terentyev, Journal of Nuclear Materials 329-333 (2004) 1175.
- 27 [37]H.J. Vanrijn, H.L. Alberts, Journal of Physics F-Metal Physics 13 (1983) 1559.
- 28 [38]R. Pasianot, D. Farkas, E.J. Savino, Physical Review B 43 (1991) 6952.
- 29 [39]O. Yifang, Z. Bangwei, L. Shuzhi, J. Zhanpeng, Zeitschrift für Physik B 101 (1996) 161.
- 30 [40]Z. Bangwei, O. Yifang, L. Shuzhi, J. Zhanpeng, Physical B 262 (1999) 218.
- 31 [41]K.W. Katahara, M. Nimalendran, M.H. Manghnani, E.S. Fisher, Journal of Physics F-
32 Metal Physics 9 (1979) 2167.
- 33 [42]V. Vitek, Crystal Lattice Defects 5 (1974) 1.

Deleted: Accepted

- 1 [43]D. Terentyev, G. Bonny, C. Domain, R.C. Pasianot, *Physical Review B* 81 (2010)
2 214106.
3
4 [44]G. Bonny, R.C. Pasianot, L. Malerba, A. Caro, P. Olsson, M.Y. Lavrentiev, *Journal of*
5 *Nuclear Materials* 385 (2009) 268.
6
7 [45]A. Zunger, S.H. Wei, L.G. Ferreira, J.E. Bernard, *Physical Review Letters* 65 (1990) 353.
8
9 [46]B.L. Gyorffy, *Physical Review B* 5 (1972) 2382.
10
11 [47]T.P.C. Klaver, G. Bonny, P. Olsson, D. Terentyev, *Model. Simul. Mater. Sci. Eng.* 18
12 (2010) 16.
13 [48]C. Pareige, C. Domain, P. Olsson, *Journal of Applied Physics* 106 (2009) [104906](#).
14 [49]B. Fultz, L. Anthony, J.L. Robertson, R.M. Nicklow, S. Spooner, M. Mostoller, *Physical*
15 *Review B* 52 (1995) 3280.
16
17 [50]T.L. Swan-Wood, O. Delaire, B. Fultz, *Physical Review B* 72 (2005) 024305.
18
19 [51]M.S. Lucas, M. Kresch, R. Stevens, B. Fultz, *Physical Review B* 77 (2008) 184303.
20 [52]G. Bonny, P. Erhart, A. Caro, R.C. Pasianot, L. Malerba, M. Caro, *Modelling and*
21 *Simulation in Materials Science and Engineering* 17 (2009) 025006.
22
23 [53]G. Bonny, D. Terentyev, L. Malerba, *Journal of Phase Equilibrium and Diffusion* 31
24 (2010) 439.
25
26 [54]J. Andersson, B. Sundman, *Calphad* 11 (1987) 83.
27 [55]G. Bonny, R.C. Pasianot, E. Zhurkin, M. Hou, in preparation (2010).
28
29 [56]G. Henkelman, H. Jonsson, *Journal of chemical physics* 113 (2000) [9978](#).
30 [57]A. Moslang, H. Graf, G. Balzer, E. Recknagel, A. Weidinger, T. Wichert, R.I. Grynszpan,
31 *Physical Review B* 27 (1983) 2674.
32
33 [58]D. Nguyen-Manh, M.Y. Lavrentiev, S.L. Dudarev, *Comptes Rendus Physique* 9 (2008)
34 379.
35
36 [59]D. Terentyev, G. Bonny, L. Malerba, *Acta Materialia* 56 (2008) 3229.
37 [60]T. Harry, D.J. Bacon, *Acta Materialia* 50 (2002) 209.
38
39 [61]D. Terentyev, G. Bonny, L. Malerba, *Nuclear Instruments & Methods in Physics*
40 *Research Section B-Beam Interactions with Materials and Atoms* 267 (2009) 3155.
41
42 [62]E. Nembach, *Physica Status Solidi A-Applied Research* 78 (1983) 571.
43
44 [63]W. Pearson, *A Handbook of Lattice Spacings and Structures of Metals and Alloys*,
45 Pergamon Press, New York, 1958.
46 [64]G. Loper, L. Smedskjaer, M. Chason, R. Siegel, *Positron Annihilation*. in: P. Jain, (Ed.),
47 *World Scientific, Singapore, 1985, pp. 461.*
48
49
50
51
52
53
54
55
56
57
58
59
60

- 1 [65]H. Schultz, Materials Science and Engineering A-Structural Materials Properties
2 Microstructure and Processing 141 (1991) 149.
3
4 [66]S. Cottenier, Private communication (2009).
5
6 [67]Y.N. Osetsky, D.J. Bacon, Modelling and Simulation in Materials Science and
7 Engineering 11 (2003) 427.
8
9 [68]D. Terentyev, D. Bacon, Y. Osetsky, Journal of Physics: Condensed Matter 20 (2008)
10 [445007](#).

11 Table and Figure Captions

12
13
14
15 **Table 1** – Summary of the basic properties of both Cr potentials.

16 **Table 2** – Properties of Fe and Cr as obtained from the potentials.

17 **Table 3** – Differential displacement maps drawn in the (111) zone, for a screw dislocation
18 interacting with a 2nm precipitate. The thick dashed line shows the edge of the precipitate and
19 a double arrow shows the directions of the preferential split of the dislocation core. The centre
20 of the dislocation core is shown by symbol §.
21
22
23

24
25 **Table B-1** – The vacancy migration barrier for different local Cr configurations, with the first
26 and second value denoting the forward and backward jump, respectively. In the figure black
27 circles are Fe, white ones are Cr, in grey is the migrating atom, and the square represents the
28 vacancy.
29

30
31 **Figure 1** – Comparison of the screw component of differential displacement maps obtained
32 with our potential (a) and the O05 potential (b).
33

34 **Figure 2** – Comparison of the mixing enthalpies obtained from the potentials with DFT data
35 [8; 12; 44].
36

37 **Figure 3** – Comparison of the formation energy obtained by the different potentials with the
38 corresponding DFT values [11; 47; 48] for various intermetallic compounds.
39

40 **Figure 4** – Comparison of the excess vibrational entropy obtained from the different potentials
41 with the experimental ones from [49; 51].
42

43 **Figure 5** – Comparison of the phase diagrams resulting from the different potentials against a
44 CALPHAD based calculation. The curves for the OLS and our potential were taken from
45 [55], while for CAR and CALPHAD they were taken from [52] and [53], respectively.
46

47 **Figure 6** – Comparison between DFT [12] and all three potentials of the interaction energy
48 between Cr-Cr and Cr-vacancy pairs in bulk Fe.
49

1 **Figure 7** – Comparison between DFT [58] and the three potentials of the average vacancy
 2 migration barrier in bulk Fe for different local Cr configurations around the saddle.
 3

4 **Figure 8** – Formation energies of different interstitial configurations in bulk Fe and Cr,
 5 calculated using DFT [12] and the three different potentials.
 6

7 **Figure 9** – Comparison between DFT [12] and the three potentials of the binding energy of Cr
 8 interstitial configurations.
 9

10 **Figure 10** – Precipitate dislocation interaction energy as function of the distance for our (left)
 11 and the OLS potential (right). The position of maximal force between precipitate and
 12 dislocation is indicated by F_{MAX} .
 13

14 **Figure 11** – Different contributions to the interaction energy (top row) and interaction force
 15 (bottom row) for our (left) and the OLS potential (right), for a 4 nm Cr precipitate. The
 16 position of the precipitate edge and maximal force between precipitate and dislocation are
 17 indicated by R_P and F_{MAX} , respectively.
 18
 19

20 Tables

21 **Table 1**

	Experiment or DFT	This Work	O05
a_0 (Å)	2.878 ^a / 2.834 ^b	2.866	2.878
B (GPa)	208 ^c	215	208
C' (GPa)	152 ^c	155	152
C_{44} (GPa)	105 ^c	108	105
E_{coh} (eV)	4.10	4.10	3.84
E_t^V (eV)	2.0 ± 0.2 ^d / 2.59 ^b	2.52	2.56
E_m^V (eV)	0.95 ^e	0.94	0.99
$E_{coh}^{fcc} - E_{coh}^{bcc}$ (eV)	-0.4 ^f	-0.16	-0.03
$E_t^{<110>} - E_t^{<111>}$ (eV)	-0.02 ^b	-0.07	-0.02
$E_t^{<110>} - E_t^{<100>}$ (eV)	-1.12 ^b	-0.58	-1.23

22 ^a Experiment, Ref. [63]

23 ^b DFT, Ref [20]

24 ^c Experiment, Ref. [41]

25 ^d Experiment, Ref. [64]

26 ^e Experiment, Ref. [65]

^f DFT, Ref. [66]

Table 2

Property	Iron		Chromium	
	OLS	This Work	OLS	This Work
Lattice unit a_0 (nm)	0.28553	0.28553	0.2878	0.2866
Core radius r_0 (b)	3	3	3	3
Core energy E_C screw (eV/nm)	4.24	4.27	6.27	6.23
Core energy E_C edge (eV/nm)	6.97	7.01	9.71	9.6
Shear modulus* μ (Gpa)	73	73	130	89
Poisson** ratio ν	0.49	0.49	0.21	0.4
Peierls stress for $\frac{1}{2}\langle 111 \rangle$ screw dislocation for the glide in a (110) plane (GPa)	1.4	1.3	1.95	2.02

* The shear modulus was estimated by straining a crystal on a $\{110\}$ plane in a $\langle 111 \rangle$ direction, as was done in Ref.[67].

** The Poisson ratio was determined following the method used in Ref.[68] for pure Fe.

Table 3

Configuration	OLS	This Work
#1		

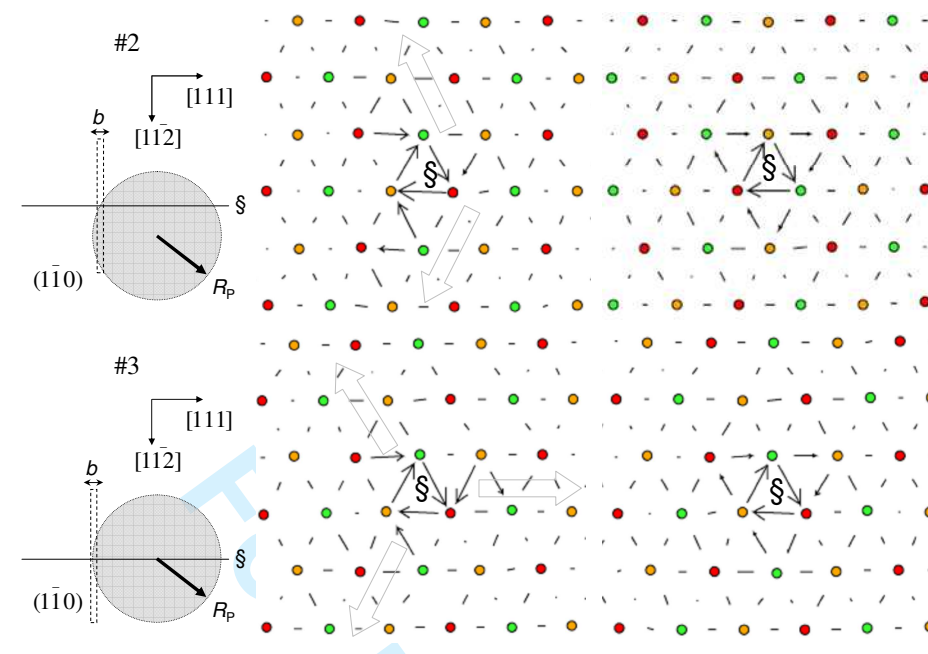
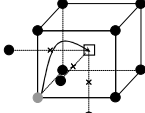
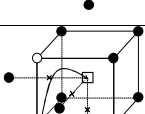
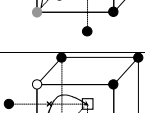
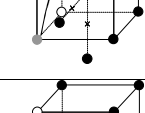
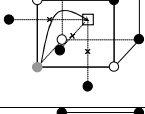
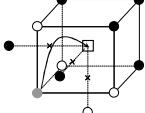
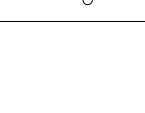



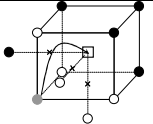
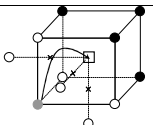


Table A-1

Configuration	DFT	This Work	OLS	CAR
	E_m^{Cr} 0.57 / 0.57	0.57 / 0.57	0.56 / 0.56	0.90 / 0.90
	E_m^{Fe} 0.64 / 0.64	0.63 / 0.63	0.64 / 0.64	0.63 / 0.63
	E_m^{Cr} 0.72 / 0.54	0.63 / 0.57	0.61 / 0.53	0.97 / 0.87
	E_m^{Fe} 0.66 / 0.60	0.65 / 0.63	0.67 / 0.63	0.64 / 0.62
	E_m^{Cr} 0.79 / 0.52	0.66 / 0.58	0.62 / 0.51	1.00 / 0.85
	E_m^{Fe} 0.73 / 0.57	0.67 / 0.63	0.68 / 0.61	0.65 / 0.61
	E_m^{Cr} 1.09 / 0.69	0.68 / 0.58	0.59 / 0.49	0.99 / 0.82
	E_m^{Fe} 0.84 / 0.55	0.69 / 0.63	0.67 / 0.60	0.65 / 0.59
	E_m^{Cr} 0.88 / 0.55	0.67 / 0.61	0.56 / 0.51	0.86 / 0.77
	E_m^{Fe} 0.78 / 0.58	0.68 / 0.64	0.66 / 0.62	0.57 / 0.55

	E_m^{Cr}	0.74 / 0.56	0.66 / 0.62	0.54 / 0.52	0.76 / 0.72
	E_m^{Fe}	0.70 / 0.61	0.67 / 0.65	0.65 / 0.64	0.50 / 0.50
	E_m^{Cr}	0.56 / 0.56	0.64 / 0.64	0.52 / 0.52	0.67 / 0.67
	E_m^{Fe}	0.64 / 0.64	0.66 / 0.66	0.64 / 0.64	0.47 / 0.47

Figures

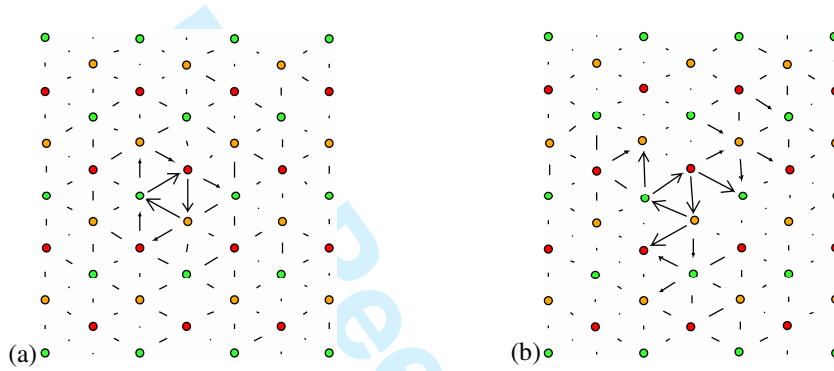


Figure 1

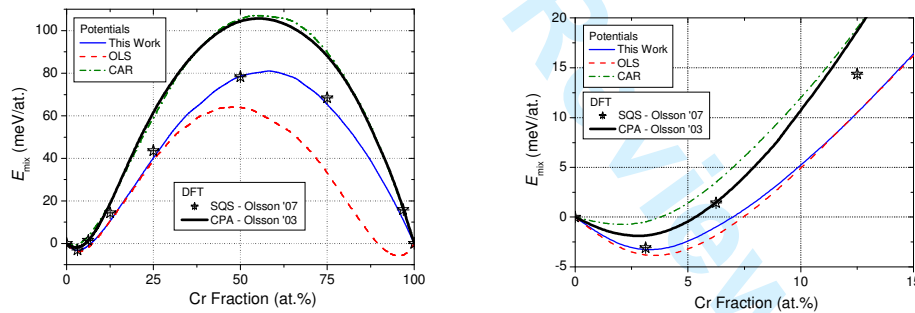


Figure 2

Formatted Table

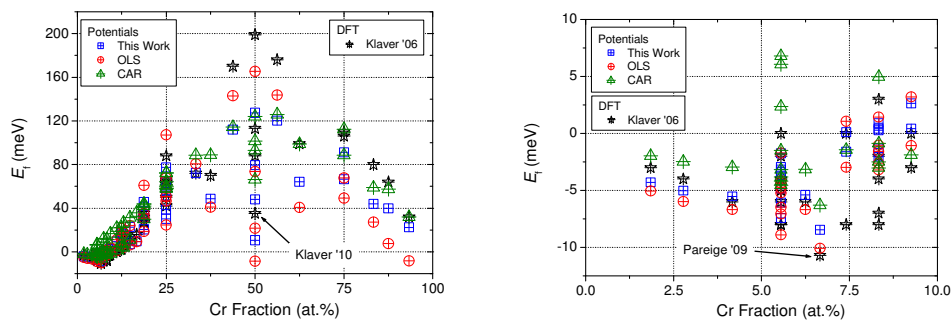


Figure 3

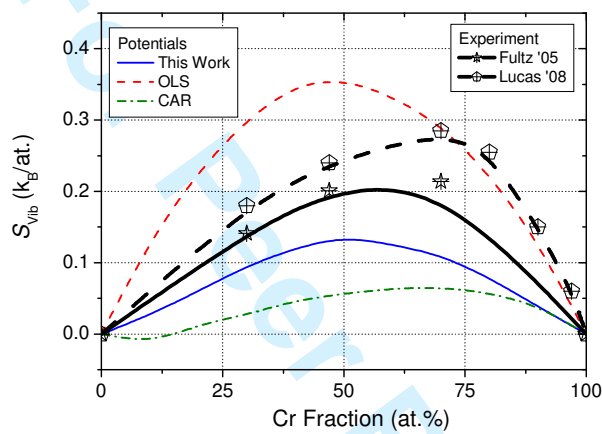


Figure 4

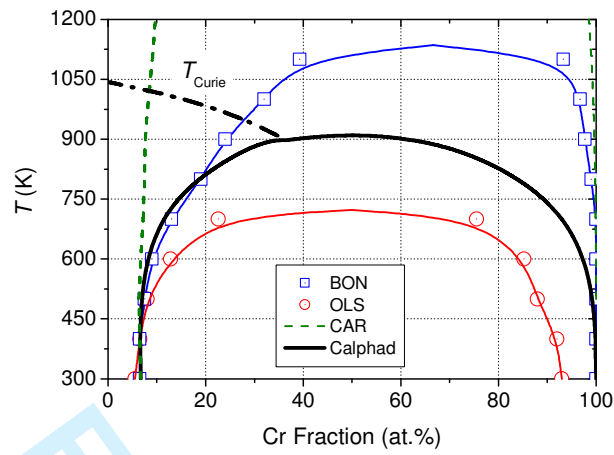


Figure 5

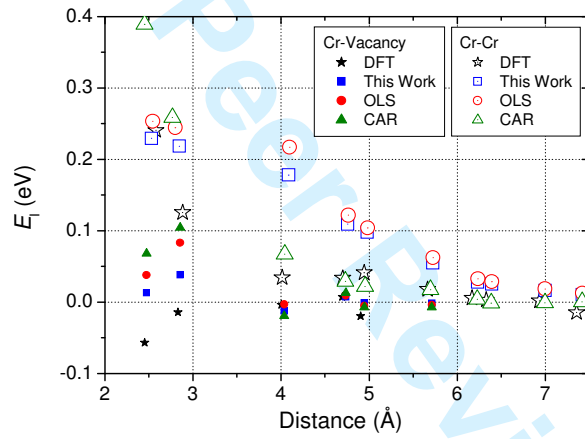


Figure 6

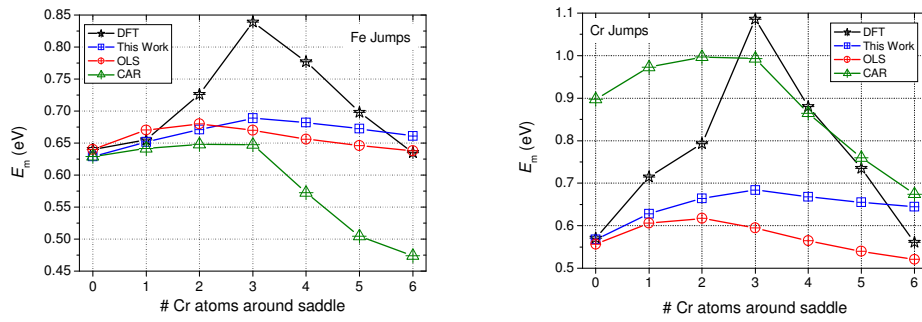


Figure 7

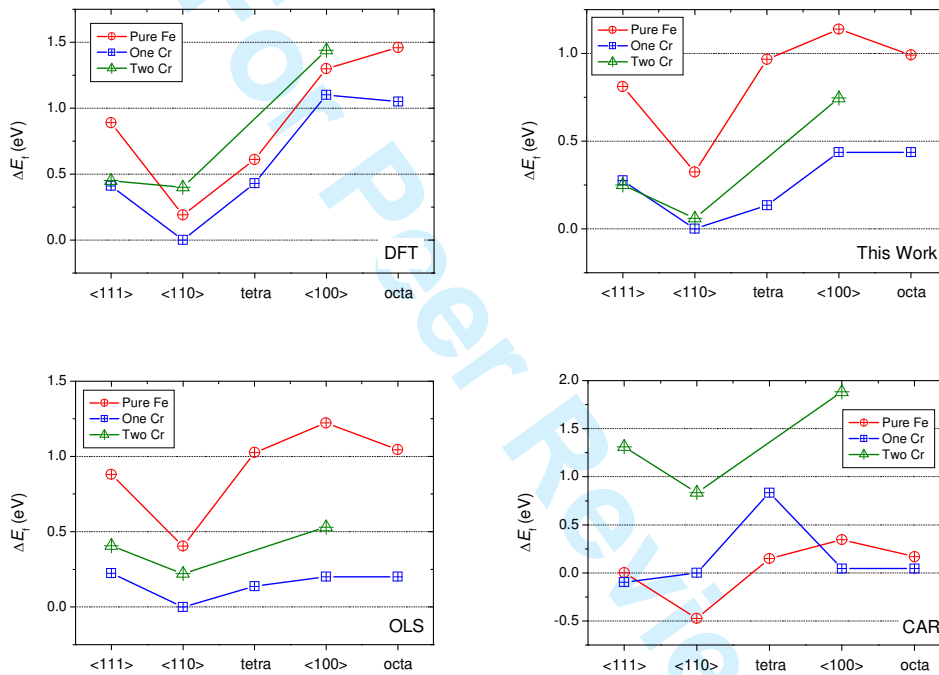


Figure 8

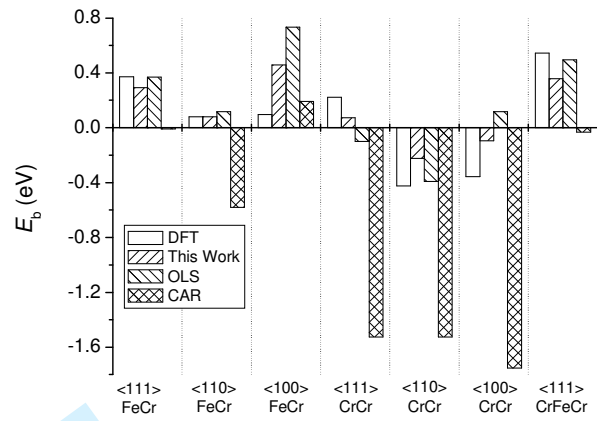


Figure 9

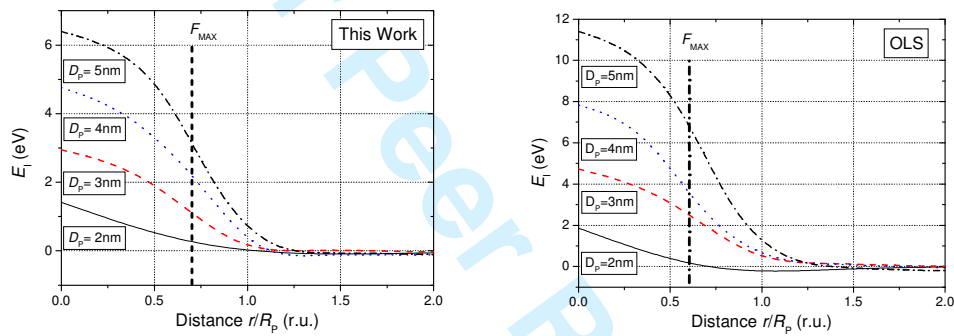
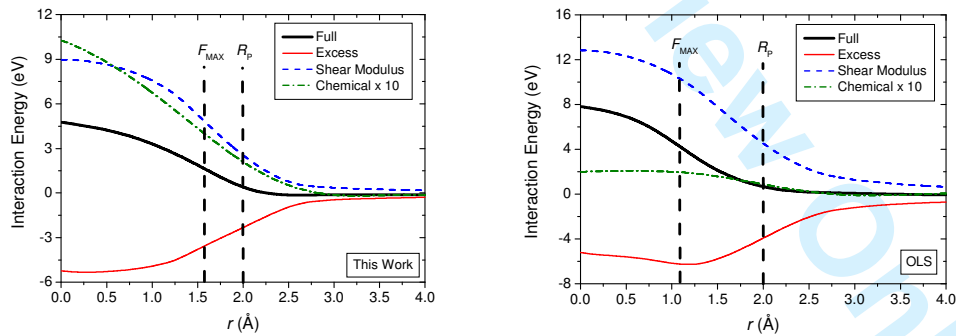


Figure 10



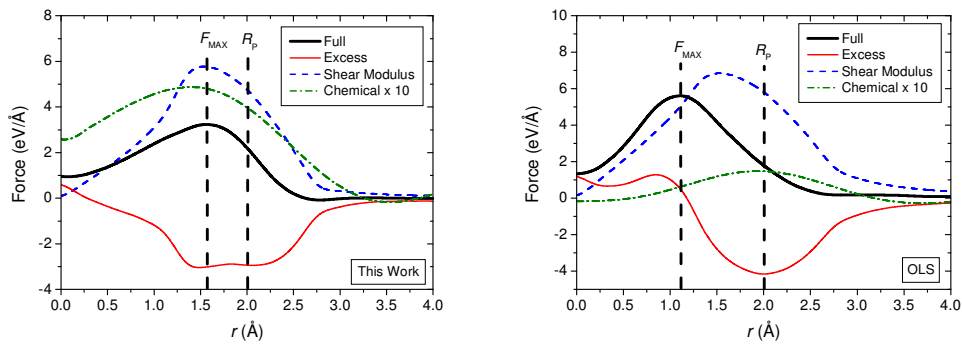


Figure 11

For Peer Review Only